

Article

Multimodal Radiobioconjugates of Magnetic Nanoparticles Labeled with ^{44}Sc and ^{47}Sc for Theranostic Application

Perihan Ünak ^{1*}, Volkan Yasakçı ¹, Elif Tutun ¹, K. Buşra Karatay ¹, Rafał Walczak ², Kamil Wawrowicz ², Kinga Żelechowska-Matysiak ², Agnieszka Majkowska-Pilip ², Aleksander Bilewicz ^{2*}

¹ Ege University, Institute of Nuclear Sciences, Department of Nuclear Applications, 35100 Bornova Izmir, Turkey;

² Centre of Radiochemistry and Nuclear Chemistry, Institute of Nuclear Chemistry and Technology, Dorodna 16 St., 03-195 Warsaw, Poland;

* Correspondence: a.bilewicz@ichtj.waw.pl (A.B.); perihan.unak@gmail.com (P. Ü.)

Abstract: This study was performed to synthesize multimodal radiopharmaceutical designed for the diagnosis and treatment of prostate cancer. To achieve this goal, Superparamagnetic Iron Oxide (SPIO) nanoparticles were used as a platform for targeting molecule (PSMA-617) and for complexation of two scandium radionuclides, ^{44}Sc for PET imaging and ^{47}Sc for radionuclide therapy. TEM and XPS images showed that the Fe_3O_4 NPs have a uniform cubic shape and a size from 38 to 50 nm. The Fe_3O_4 core are surrounded by SiO_2 and an organic layer. The saturation magnetization of the SPION core was 60 emu/g. However, coating the SPIONs with silica and polyglycerol reduces the magnetization significantly. The obtained bioconjugates were labeled with ^{44}Sc and ^{47}Sc , with a yield higher than 97%. The radiobioconjugate exhibited high affinity and cytotoxicity towards the human prostate cancer LNCaP (PSMA+) cell line, much higher than for PC-3 (PSMA-) cells. High cytotoxicity of the radiobioconjugate was confirmed by radiotoxicity studies on LNCaP 3D-spheroids. In addition, the magnetic properties of the radiobioconjugate should allow for its use in guide drug delivery driven by magnetic field gradient.

Keywords: SPION; multimodal nanoparticles; PET diagnosis; MRI; $^{44/47}\text{Sc}$; PSMA-617; prostate cancer

1. Introduction

In nuclear medicine nanoparticles (NPs) with magnetic properties can be used for imaging, diagnosis, treatment, and separation of biological materials [1]. Initial studies on patients with magnetically controlled drug targeting were reported by Lübke et al. The authors stated that 0.5-0.8 Tesla magnetic field intensity is sufficient to direct iron nanoparticles to tumors near the surface [2]. It is also possible to target drugs to diseased tissue by loading drug molecules on magnetic particles. Magnetic nanoparticles (MNPs) can also be labeled with radionuclides, what enable them to be used in radiopharmacy. MNPs may be advantageous in alpha radionuclide therapy as retain ^{225}Ac and its daughter products at a target site. Cedrowska et al reported that radiolabeled iron oxide nanoparticles with Ac-225 and modified with CEPA-Tmab were proposed for a combination of magnetic hyperthermia and radionuclide therapy [3]. In another publication ^{223}Ra -doped BaFe nanoparticles were presented as candidates for multimodal drug combining localized magnetic hyperthermia with internal α -therapy [4]. Magnetic nanoparticles labeled also with β -emitters (^{188}Re , ^{198}Au , ^{90}Y , and ^{131}I) and Auger electrons emitters (^{111}In , ^{125}I) were also investigated, some of them in preclinical studies [5–9].

MNPs in medicine can be classified as therapeutic (hyperthermia and drug targeting) and diagnostic (NMR imaging) agents. Shape and size, biocompatibility, and stability of nanoparticles are parameters to be considered. Silica coating prevents magnetic nanoparticles from aggregating uncontrollably and oxidizing over time. TEOS (tetraethyl orthosilicate) is one of the most commonly used methods although there are different coating

methods [10]. The silica layer stabilizes the MNP core by sustaining magnetic dipole interactions. In medical applications, MNPs can be coated with a biocompatible polymer to increase stability and bioavailability [11] or coated with antibody for biomarker immobilization [12]. Among others, MNPs modified with Hyperbranched Polyglycerol (HPG) have attracted much attention for years [1–11,13–15]. Having three-dimensional structures and numerous internal and external functional groups, these compounds can serve as remarkable hosts for metal complexes, enzymes, and biomaterials. HPG has many reactive functional groups that can be converted to other functional groups. In addition, HPG-modified MNPs have been used in various applications such as magnetic resonance imaging (MRI), drug delivery, and catalysis [16].

In our work, we have designed a multifunctional agent combining PET and MRI imaging and radionuclide therapy using SPION nanoparticles as a platform [12]. A prostate-specific membrane antigen (PSMA) molecule will be implemented for targeting, while a DOTA chelator incorporated into the PSMA-617 structure will be used to complex two scandium radionuclides ^{44}Sc for PET diagnosis and ^{47}Sc for therapy.

The PSMA small molecule is an antagonist with a very high affinity to specific membrane antigens expressed in aggressive prostate cancer. Due to the high resistance of this tumor, it is recommended to use several therapeutic methods, e.g., chemo- and radiotherapy during treatment. The second therapeutic method that we planned to use is the so-called magnetic hyperthermia. The therapeutic effect obtained will result from the impact of β - radiation emitted by ^{47}Sc radiation as well as from local hyperthermia - heating of cancer cells to a temperature above 42°C , induced by fast oscillations of SPIONs in an external alternating magnetic field. Covalent binding of vector molecules – PSMA for further radiolabeling in the final step of synthetic processes to the SPIONs will provide a precise, targeted delivery of obtained radiobioconjugate only to the selected tumor cells overexpressing PSMA receptors, while the external alternating magnetic field causing an increase temperature will multiply the therapeutic effect.

It is well known that prostate cancer can spread to any part of the body, but most commonly, metastatic sites are directed to the bones [17]. Nuclear medicine aims to treat bone metastases with ^{153}Sm Sm-EDTMP or ^{177}Lu Lu-EDTMP, while $^{99\text{m}}\text{Tc}$ Tc-MDP are mainly used in the imaging of bone metastases [18]. Phosphate derivatives such as EDTMP and DPAPA may be suitable targeting agents for theragnostic, where imaging and treatment with the same agent are used together. In this work, we added to HPG-modified MNPs two phosphonate derivatives EDTMP or DPAPA, for targeting of prostate cancer and its metastases. With PSMA-617, we present a compound that, in addition to a PSMA inhibitor as a target vector, also contains a bisphosphonate that is established as a bone tracer and thus combines the advantages of PSMA targeting and bone targeting.

Additionally, due to their superparamagnetic behavior, radionuclide labeled SPIONs bioconjugates can be guided and retained exclusively in the tumor tissue with help of an external constant magnetic field. Their accumulation in this tissue can be followed by functional NMR and positron emission tomography (PET). Thus, we proposed a promising radionuclide therapy and imaging tool as an "All-in-One" approach.

2. Materials and Methods

2.1. Reagents and Instruments

Iron(III) acetylacetonate [$\text{Fe}(\text{acac})_3$; $\text{Fe}(\text{C}_5\text{H}_7\text{O}_2)_3$; 97%], decanoic acid [$\text{CH}_3(\text{CH}_2)_8\text{COOH}$; 98%], benzyl ether [$(\text{C}_6\text{H}_5\text{CH}_2)_2\text{O}$; 98%], tetraethyl orthosilicate [TEOS; $(\text{C}_2\text{H}_5\text{O})_4\text{Si}$; for synthesis], potassium methylate (CH_3OK ; for synthesis), anhydrous methanol (CH_3OH ; 99.8%), glycidol ($\text{C}_3\text{H}_6\text{O}_2$; 96%), ethylenediamine ($\text{NH}_2\text{CH}_2\text{CH}_2\text{NH}_2$; absolute, $\geq 99.5\%$), sodium cyanoborohydride (NaBH_3CN ; reagent grade, 95%), N-ethyl-N'-(3-dimethylaminopropyl)carbodiimide hydrochloride [E.D.C.; $\text{C}_8\text{H}_{17}\text{N}_3$ hydrochloric acid (HCl) Bio extra], N-hydroxy succinimide ($\text{C}_4\text{H}_5\text{NO}_3$; 98%), 3-(4,5-dimethylthiazol-2-yl)-2,5-diphenyltetrazolium bromide (MTT; 98%), dimethyl sulfoxide (DMSO), and trifluoroacetic acid [TFA; CF_3COOH ; high-performance liquid chromatography (HPLC), 99%] were

obtained from Sigma-Aldrich (Taufkirchen, Germany). Acetonitrile (HPLC grade) was purchased from Carlo Erba Reagents (Barcelona, Spain). Dulbecco's modified Eagle's medium (DMEM), fetal bovine serum (FBS), penicillin/streptomycin solution, RPMI-1640, L-glutamine, trypsin-EDTA, nonessential amino acids, sodium pyruvate, and phosphate-buffered saline (PBS) were acquired from Biowest (Nuaille, France). Muse® Annexin V & Dead Cell Kit and Instrument Cleaning Fluid were purchased from Luminex (Northbrook, IL, USA). HCl (37%), phosphoric acid, and sodium hydroxide were supplied by Merck KGaA (Darmstadt, Germany). Deionized water was processed in a Milli-Q water purification system.

PC-3 [PSMA (-) human prostate derived from the metastatic part of the bone], LNCaP [PSMA (+) prostate derived from the metastatic site left supraclavicular lymph node] cells were supplied by the American Type Culture Collection (ATCC; Manassas, VA, USA). These cells were obtained from the ATCC using the authors' previous project resources for academic studies in the cell culture laboratory of the Ege University Institute of Nuclear Sciences.

Hydrochloric acid 35-38%, analytical pure, Chempur, Poland; Ammonium Acetate, analytical pure, Chempur, Poland; Ammonia solution 25%, analytical pure, Chempur, Poland; Human serum, Sigma-Aldrich, USA; Dulbecco's PBS, Biological Industries, Israel; Calcium Carbonate 4,3% ⁴⁶Ca, Isoflex, USA; Calcium Carbonate, 99,999%, Alfa Aesar, USA; Syringe filter 0.2 µm, PTFE Whatman, Great Britain; Cation exchange resin Dowex 50WX4, mesh 100-200, H+, Fluka Analytical, USA

Following materials were used: growing medias – DMEM (PC-3) and RPMI 1640 (LNCaP); Trypsin EDTA solution C; water, cell culture grade; phosphate-buffered saline (PBS) and fetal calf serum from Biological Industries (Beth Haemek, Israel). For cytotoxicity evaluation, CellTiter96® AQueous One Solution Reagent (MTS compound) from Promega (Mannheim, Germany) was used. LNCaP and PC-3 cells were obtained from the American Type Tissue Culture Collection (ATCC, Rockville, MD, USA) and cultured accordingly to the ATCC protocol. For experimental applications, over 80% confluent cells were used. Blocking the PSMA receptors was accomplished with PSMA-617, obtained from Selleck Chemicals L.L.C., Houston, TX USA.

The following equipment was used: HPLC SPD-10AV ultraviolet-visible (UV-vis) and AD2 detector systems with an LC-10Atvp pump (Shimadzu, Kyoto, Japan), Inertsil ODS-3 C-18 4.6 250 mm HPLC 5 µm column (G.L. Sciences, Inc., Tokyo, Japan), SIL-20A HT automatic sampler (Shimadzu), Varioskan Flash multimode microplate reader (Thermo Fisher Scientific, Darmstadt, Germany), AR-2000 radioTLC (thin-layer radiochromatography) imaging scanner (Eckert & Ziegler, Berlin, Germany), Packard Tricorb-1200 liquid scintillation counter (Meriden, CT, USA), Malvern Zetasizer Nano ZS dynamic light scattering (D.L.S.; Malvern Panalytical, Malvern, U.K.), Millipore Muse Dead Cell Analyzer Flow Cytometry inverted microscope (Leica Microsystems, Wetzlar, Germany), and Spectrum Two I.R. spectrophotometer (attenuated total reflection; Perkin-Elmer, Boston, MA, USA). The Ege University Central Research Laboratory was supplied for the below analyses:

X-ray photoelectron spectroscopy (XPS) analysis was done with the K-Alpha XPS System (Thermo Fisher Scientific, U.K.). The scanning probe microscopy (S.P.M.) image was taken by a Bruker Dimension Edge with ScanAsyst System (Billerica, MA, USA). Scanning electron microscopy (SEM) images were taken with the Thermo Scientific Apreo S device at the Ege University Central Research Laboratory and the SEM Zeiss EVO LS10 (Carl Zeiss Microscopy GmbH, Germany) at the Konya Selçuk University Advanced Research Center (Iltak). ¹H-NMR, ¹³C-NMR and ³¹P-NMR spectra of DPAPA were performed with the 400 MHz operating frequency liquid MERCURY plus-AS 400 model NMR spectrometer in the Nuclear Magnetic Resonance Laboratory of Ege University Faculty of Science. Transmission electron microscopy (TEM) measurements were made with a JEOL-2100 Multipurpose 200 kV TEM (Tokyo, Japan) at the Advanced Research and Application Centre of Konya Selçuk University (Konya, Turkey). Vibrating sample magnetometer (V.S.M.) measurements were done at the Dokuz Eylül University Centre for Fabrication

and Application of Electronic Materials using Dexion Magnet VSM 550 devices, ICP-MS analyses were performed the Agilent Technologies 7800 Series device, C.A., United States in Izmir Katip Çelebi University Central Research Laboratory (MERLAB).

2.2. Cubic Fe_3O_4 (C- Fe_3O_4) NP Synthesis.

Fe_3O_4 nanocubes were prepared according to the procedure described by Martinez-Boubeta et al [19] involving heating a solution of $\text{Fe}(\text{acac})_3$, decanoic acid, and dibenzyl ether. This method is done by the discriminant separation of nucleation and growth stages caused by the intermediate formation of the iron(III) decanoate complex, as discussed previously [19].

2.3. Silica and HPG Coating of C- Fe_3O_4 NPs and Ethylenediamine Coupling

Silica coating of C- Fe_3O_4 NPs was performed using the procedure described previously [20]. The HPG coating was made according to the method proposed by Sadri et al [21]. The synthesis path of ethylenediamine coupling with Fe_3O_4 - SiO_2 -HPG in the literature has been realized with modifications [22].

2.4. Synthesis of DPAPA and Conjugation with Fe_3O_4 - SiO_2 -HPG- NH_2

DPAPA was synthesized using a modified Mannich-type reaction according to the method given in the literature described for EDTMP [23] (Figure 1). Synthesized cubic MNPs were conjugated with DPAPA using the EDC/(N-(3-dimethyl aminopropyl)-N'-ethyl carbodiimide hydrochloride/N-hydroxy succinimide (NHS) conjugation method [20].

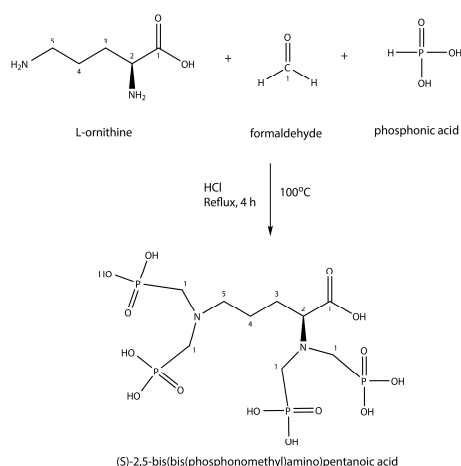


Figure 1. DPAPA synthesis reactions (Mannich-type reaction).

2.5. Production of $^{44/47}\text{Sc}$

^{44}Sc : CaCO_3 (88.87 mg, 99.999 % purity) target material was pressed into 6 mm disc, supported on graphite. The target was irradiated by 16 MeV proton with 14 μA current on GE-PET trace 840 cyclotron at Heavy Ions Laboratory, Warsaw University. The irradiation was carried out for 100 minutes.

^{47}Sc : ^{47}Sc was produced in $^{46}\text{Ca}(n,\gamma)^{47}\text{Ca} \rightarrow ^{47}\text{Sc}$ reaction in Nuclear Reactor – Maria in Świerk (Otwock, Poland). 5 mg of CaCO_3 (4.3% ^{46}Ca) was irradiated for 120 h with 10^{14} n/cm²s thermal neutron flux. After irradiation target was cooled for 5 days to reach the maximum activity of ^{47}Sc produced from ^{47}Ca decay. 5 days after the irradiation 90 MBq of ^{47}Sc was produced from ^{47}Ca decay.

2.6. Separation Procedure

For the separation of $^{44/47}\text{Sc}$ from the target material two-step method based on microfiltration [24] and cation exchange on Dowex resin was used [25]. First, the irradiated target was dissolved in 1 M HCl, and then the solution was alkalized with the ammonia solution (25%) to pH ~ 11. In these conditions, Sc compounds were trapped on 0.22 μm porous microfilters. The loss of radionuclides after this process was no higher than 10%. For the removal of Ca tracers microfilter was washed with 5 mL of deionized water. After that scandium cations were removed from filters with 2 mL 1 M HCl with efficiency $84.6 \pm 0.75\%$ and load on 200 mg of Dowex 50WX4 cation exchange resin. Bed was washed with 5 mL water for removal of residual HCl with almost no loss of the activity. Elution of Sc from DOWEX resin was performed with 0.4 M ammonium acetate buffer, pH 4.5, 0.5 mL/min flow and the eluent was collected with 0.5 mL fractions.

2.7. Radiolabeling with $^{44/47}\text{Sc}$

After the separation process $^{44/47}\text{Sc}$ was in 0.4 M ammonium acetate buffer, pH 4.5, which is a suitable environment for labeling of DOTA chelator. 1 mL of nanoparticles (41 mg of NP) were centrifuged 4500 rpm for 5 min. After that, supernatants were removed and replaced with 100 μL of 1 M ammonium acetate buffer. Next, 30 MBq of ^{44}Sc or ^{47}Sc in ammonium acetate buffer were added to EDTMP-PSMA NCs or DPAPA-PSMA NCs and incubated for 30 minutes at 95°C . After incubation, the samples were centrifuged to remove the unbound $^{44/47}\text{Sc}$ from the nanoparticles and their activities were measured. In every case efficiency of labelling was higher than 97%.

2.8. Stability Tests of $^{44/47}\text{Sc}$

Stability tests were performed for EDTMP PSMA NP's and EDTMP PSMA NPs labeled with ^{44}Sc . After labeling, NPs were purified from non-attached scandium and divided into two parts. Stability of bonding between Sc and NPs were checked in 500 μL Human Serum (HS) or Phosphate Buffered Saline (PBS). Samples were incubated at 37°C and the stability was checked after 1, 2, 3, 4, 24 h. After incubation at 37°C nanoparticles were centrifuged and the activity was measured.

2.9. In Vitro Studies

PC-3 (PSMA-) prostate cancer cell line, LNCaP (PSMA+) Prostate cancer cell line was used for cell culture studies. These cells were obtained from the American Type Culture Collection (ATCC) (USA) using our previous project resources for academic studies at Ege University Institute of Nuclear Sciences Cell culture laboratory. PC-3 was grown in medium consisting of Dulbecco's Modified Eagle's- Medium (DMEM) and 10% fetal bovine serum (FBS). LNCaP was grown in medium consisting of Roswell Park Memorial Institute RPMI-1640 Medium and 10% fetal bovine serum (FBS). Cells were incubated in 5% CO_2 and 37°C . The medium was changed every 2 days and fresh medium was added. After the cells proliferated to cover 80% of the flasks, they were separated from the flask with 0.25% (W/V) trypsin-EDTA solution and planted in 96-well plates for cytotoxicity studies. Cells that will not be used in the study were placed in media containing 5% DMSO, first frozen at below 80°C , then stored in liquid nitrogen at below 198°C and stockpiled for further studies and possible risks. All cell culture studies were performed in 6 replicates ($n=6$).

2.9.1. Cell Binding of ^{44}Sc Labeled Bioconjugates

^{44}Sc : Receptor binding affinity of synthesized bioconjugates was performed with LNCaP cells overexpressing PSMA receptors as well as, with PC-3 cells (PSMA-negative) used as control. Two days before the experiment, cells (8×10^5 LNCaP and 5×10^5 PC-3 cells, respectively) were seeded into six-well plates and incubated in 37°C with 5% CO_2 atmosphere. Subsequently, prior tested compounds were added, the cells were washed once with PBS. Next, one mL of various concentrations (0.06 – 2.0 nM) of bioconjugates

labeled with ^{44}Sc (25-30 MBq) suspended in a growing medium were added and incubated for 2 h with slight shaking. Further, the medium was aspirated, and cells were rinsed with PBS twice to remove unbound fraction. In the last step, the cells (bound fraction) were lysed twice with 1M NaOH, and all fractions were measured by Wizard2 Detector Gamma Counter (Perkin Elmer, Waltham, MA, USA). For evaluation of nonspecific binding, PSMA receptors were blocked with 2000-molar excess of non-conjugated PSMA. To calculate the specific binding, difference between total and nonspecific binding was quantified. Presented results (mean with SD) contain the data from two individual experiments, wherein each sample was repeated twice.

2.9.2. MTT Assay

Cytotoxicity tests were performed using the MTT (3-[4,5-dimethylthiazol-2-yl]-2,5 diphenyl tetrazolium bromide) method. The MTT test is based on the conversion of MTT into formazan crystals by living cells, which determines mitochondrial activity [18]. Because total mitochondrial activity correlates with the number of viable cells for most cell populations, this assay is widely used to measure the *in vitro* cytotoxic effects of drugs on cell lines or primary patient cells. Cells were prepared from cell suspensions at 5×10^4 cells/mL per well of 96-well plates. 100 μL of cell suspension was added to each well created, and a solution containing the sterile substance at six different (1, 3, 10, 30, 100 and 300 $\mu\text{g/mL}$) concentrations was added to the wells except the control. Cell and the reagent-free medium were used as a negative control. In the study, each parameter was studied with $n=5$ repetitions. The plate with the cells was incubated at 37°C in 5% CO_2 . At the 24th, 48th and 72nd hours of the incubation of the cells (PC-3, LNCaP), 10 μL of MTT solution was added to each well and incubated for 4 hours. Next, after 4 hours of incubation, instead of removing MTT, 100 μL of S.D.S. (sodium dodecyl sulfate) was added and incubated at 37°C for 24 hours in a 5% CO_2 environment. Cells were read using a spectrophotometer for the absorbance value of each well at a wavelength of 540 nm and a reference range of 690 nm.

2.9.3. MTS Assay

Cytotoxicity studies with ^{47}Sc were performed with MTS assay according to the previously reported protocol [5]. LNCaP (10×10^3) and PC-3 (7.5×10^3) cells were seeded into 96-well plates 48 h before treatment and incubated in 37°C with 5% CO_2 -supplemented atmosphere. Subsequently, the media was replaced with tested compounds labeled with ^{47}Sc and suspended in a growing medium. Cells were incubated with nanoparticles for 48 h and 72 h. Following incubation, media was removed, and fresh media was added. Finally, 20 μL of CellTiter96®Aqueous One Solution Reagent (Promega, MDN, USA) was added for 2h incubation. Absorbance was measured at 490 nm to calculate the % of metabolically active cells. IC₅₀ was calculated with using GraphPad Prism v.8 Software (GraphPad Software, San Diego, CA, USA).

2.9.4. 3D Cell Culture Studies

"Hanging Drop Model" was used for 3D cell culture using with LNCaP (PSMA+) Prostate cancer cell line and PC-3 (PSMA-) prostate cancer cell line. LNCaP is amplified in a medium consisting of Roswell Park Memorial Institute RPMI-1640 Medium and 10% fetal bovine serum (FBS), while PC-3 is derived from Dulbecco's Modified Eagle's Medium (DMEM) and 10% fetal bovine serum (FBS). Cells were incubated in 5% CO_2 and 37°C . The medium was changed every 2 days, and fresh medium was added. After the cells have proliferated to cover 80% of the flasks, they are separated from the flask with 0.25% (W/V) trypsin-EDTA solution, and the confluent cell lines are first removed from the surface for 3D cell culture. After being removed and taken into the relevant medium, the total droplet volume was prepared as 50 μL and 50,000 cells, and 3D cell culture models were created in the "hanging drop plate". The media of the drops containing the cell population were changed every day and spheroid formation was completed at the end of

the 48th hour. After the spheroid was formed, fixation was performed to obtain a 3D cell image.

The formed spheroids were transferred into the chamber slide through the relevant medium. Then it was washed with 200 μ L of PBS, 200 μ L of paraformaldehyde was added and incubated at 4°C for 30 minutes. At the end of the incubation, three washes were performed with 200 μ L of PBS at 5-minute incubation intervals. Then, 200 μ L of triton-100 was added to the cell lines and incubated for 30 minutes at room temperature. After this stage, 100 μ L (29 μ g) of DPAPA NC, PSMA-DPAPA NCs; 100 μ L (4.5 μ g) of EDTMP NC and PSMA-EDTMP NCs were added separately for each cell line chamber and the cells were incubated for 2 hours in 5% CO₂ and 37°C. After 2 hours, the applied substances were removed from the medium and washed 3 times with PBS, and finally, 2 μ L/mL DAPI was added, and the related cell images were taken using a fluorescent microscope with a fluorescent microscope (Olympus BX53) 10X green filter. At the same time, cell images were taken using the "Confocal Microscopy 3D Fluorescent Imaging (Zeiss LSM880, Cambridge, United Kingdom)".

2.9.5. MRI Imaging of PC-3 and LNCaP Cells with Nanoconjugates

MR Imaging of PC-3 and LNCaP cells incorporated with C-Fe₃O₄ nanoconjugates were taken at T2 phase using Siemens Verio 3T MRI Scanner (GmbH, Ettlingen, Germany) equipped with 640 mT/m ID 115 mm gradient. Nanoparticles and nanoconjugates encoded with 1, 2, 3, 4* were added to LNCaP (PSMA+) prostate cancer cell line, PC-3 (PSMA-) prostate cancer cell line, respectively.

2.10. Statistical Analysis

Statistical analyses were performed using GraphPad Prism software version 8.0 for Windows (GraphPad Software, San Diego, CA, USA). To evaluate whether the collected numerical data are normally distributed to compare four unpaired groups, Kolmogorov-Smirnov normality tests were applied. The comparison of means between separate groups of numerical variables was performed using a one-way analysis of variance (ANOVA). Nonlinear regression analysis was performed with the GraphPad statistical program using the cytotoxicity (%) values. With this analysis, the IC₅₀ (dose leading to death of 50% of the current cell population) values on the cell lines of all applied substances were determined.

3. Results and Discussion

3.1. Synthesis and Characterization of the Nanoparticles and Nanoconjugates

PSMA-DPAPA/EDTMP NC as a magnetite bases nanoconjugate was synthesized to develop a multifunctional theranostic agent for imaging and therapy. First, cubic Fe₃O₄ covered with a layer of silica, was synthesized. Silica coating was made to increase the colloidal stability and biocompatibility of core Fe₃O₄ NPs. HPG, as a biocompatible, multifunctional, hyperbranched dendrimer polymer, was added to the structure to increase the biocompatibility and stability of the nanoconjugate [16]. The obtained samples were characterized by SEM and TEM microscopy. According to SEM and TEM images, C-Fe₃O₄ NPs (Figure 2A) were uniform homogeneous cubic crystal shaped with a particle size of about 38-50 nm similar to previously reported images of cubic NPs [19]. According to SEM images (Figure 2B) the shapes of C-Fe₃O₄-SiO₂ NPs differ comparing to C-Fe₃O₄. This may depend on the result of the silica coating. In addition, SEM images of C-Fe₃O₄-SiO₂-HPG samples show polymeric structure related to HPG modification (Figure 2C).

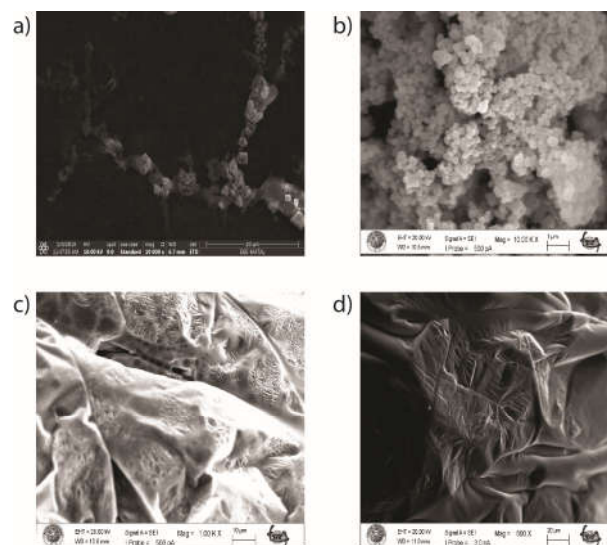


Figure 2. SEM image of obtained nanoparticles and nanoconjugates: (A) C-Fe₃O₄ SEM image, (B) C-Fe₃O₄-SiO₂ SEM image, (C) C-Fe₃O₄-SiO₂-HPG SEM image, and (D) DPAPA NC SEM image.

Figure 2 shows SEM images of (A) C-Fe₃O₄ nanoparticles, (B) C-Fe₃O₄-SiO₂, (C) C-Fe₃O₄-SiO₂-HPG and (D) DPAPA NCs. SEM images of C-Fe₃O₄ NPs showed that the cubic NPs agreed with previous reports (Figure 2A) [19]. High-density hydroxyl (–OH) groups on the outer surface of core Fe₃O₄ NPs represent the main source of reactive groups for the subsequent chemical surface. These hydroxyl groups on the surface of the nanoparticle core are combined with the silicic acid which are formed directly from sodium silicate, which polymerizes with the decrease in pH during the silication step. As a result, the resulting silanol groups (Si–OH) were condensed into covalent siloxane bonds (Si–O–Si) leading to the formation of the silica coating layer surrounding the particle core [26]. Moreover, silicated C-Fe₃O₄ nanoparticles do not aggregate easily as they exhibit higher stability compared to uncoated nanospheres. Therefore, the surface of C-Fe₃O₄-SiO₂ NPs differ from C-Fe₃O₄ NPs according to SEM images (Figure 2B). SEM images of C-Fe₃O₄-SiO₂-HPG also show the polymeric structure of HPG on the surface (Figure 2C) since HPG is a glycerol-derived polymer with a large molecular structure. HPG-coated NPs had wrinkled and folded structures with polymers covering the NP surfaces in the SEM image. Similar SEM images were given in studies with HPG [27]. DPAPA NC SEM image (Figure 2D) shows that DPAPA binds to C-Fe₃O₄-SiO₂-HPG, forming a less porous and more planar morphology. However, in closer images, the porous structure formed on the polymer surface seen due to the structural properties of DPAPA.

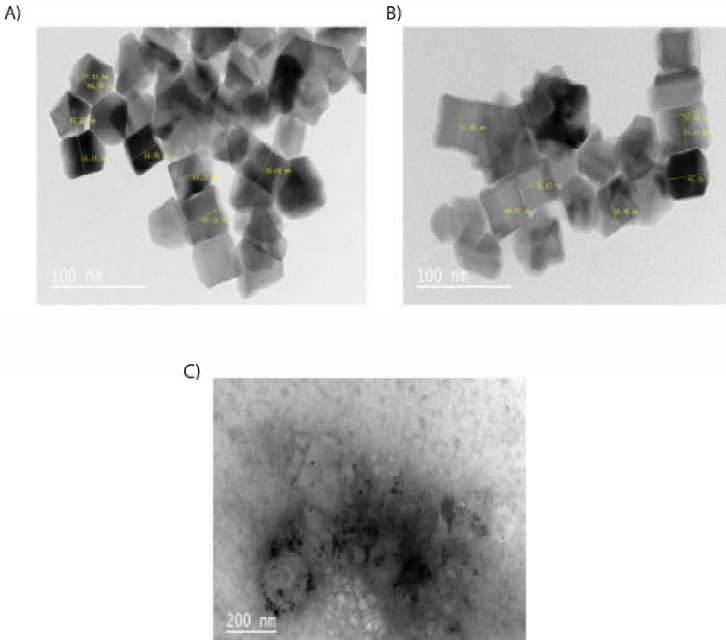


Figure 3. TEM images of NPs and nanoconjugates: (A) C-Fe₃O₄ NPs, (B) cubic silica-coated Fe₃O₄ NPs, and (C) cubic HPG-modified and silica-coated Fe₃O₄ NPs.

Figure 3 shows the TEM images of C-Fe₃O₄ (A), C-Fe₃O₄-SiO₂ (B), and C-Fe₃O₄-SiO₂-HPG (C), which are compatible with cubic Fe₃O₄ images in the literature [19]. Dark areas or black spots seen in TEM images belong to the Fe₃O₄ core, whereas the colorless parts belong to silica and HPG polymer due to their lower electron density. Iron gives a more intense appearance compared to other phases. In addition, Fe₃O₄ NPs are uniform cubic shaped with a size from 38 to 50 nm. TEM images showed that the Fe₃O₄ core is surrounded by SiO₂ and organic phase.

The hydrodynamic diameters, zeta potentials and PDI values of the nanoconjugates are given in Table 1. Hydrodynamic sizes of C-Fe₃O₄ NPs were found to be 116 nm, as agree with other reports [28] and increases when the nanoparticles are covered with layers of SiO₂, HPG and DPAPA. Hydrodynamic sizes involve the solvent molecules around the nanoparticles therefore are usually measured larger than the dimensions measured by SEM and TEM images. The size distribution of the samples is expressed by the PDI value, where the PDI value and the size homogenization are inversely proportional [29]. The data presented in Table 1 is consistent with the literature [30] and indicates homogenous population of nanoconjugates.

Table 1. Hydrodynamic sizes and zeta potentials of C-Fe₃O₄ NPs and nanoconjugates (n=6).

Nanoconjugate	Hydrodynamic size (d.nm) (n=3)	Zeta Potential (mV) (n=3) (pH=7)	PDI
C-Fe ₃ O ₄	116 ± 7.90	-18.6 ±0.60	0.13
C-Fe ₃ O ₄ -SiO ₂	122 ± 0.20	-21.5 ±0.01	0.22
C-Fe ₃ O ₄ -SiO ₂ -HPG	145.8 ± 3.50	-18.5 ±0.20	0.15
DPAPA NC	221.9 ± 16.00	-24.2 ±0.30	0.06

Zeta potentials (ζ) provide information about the charge distribution on the surface of the nanoconjugates. In general, absolute zeta potential values above 30 mV provide good stability and about 20 mV provide only short term stability, which is generally considered as a threshold value for the electrostatic stabilization, values in the range -5 mV to +5 mV indicate fast aggregation [31,32]. We performed zeta potential measurements at three various pH (pH=2, pH=7 and pH=12), where at 2 and 12 the hydrodynamic diameter of the NPs did not show any significant changes. Based on literature data, zeta potential values became increasingly negative as the pH value increased [33–35]. At physiological

pH (pH = 7.0), the zeta potential value of the DPAPA NC is -24.2 ± 0.30 mV indicating threshold colloidal stability. At pH=2, colloidal stability was lost, and zeta potential values of nanoconjugates were $+3.20 \pm 0.40$ mV and $+5.40 \pm 0.50$ mV for C-Fe₃O₄-SiO₂-HPG and DPAPA NC, respectively. In addition, the C-Fe₃O₄-SiO₂-HPG and DPAPA NCs had a zeta potential of -29.10 ± 4.10 and -38.80 ± 3.40 mV at pH=12, which can be attributed to the -OH groups of HPG molecule. Obtained zeta potential values in a function of pH confirm the presence of amine-decorated HPG on the MNP surface. For aminated HPG-coated MNPs, the particles had higher potential because the introduction of aminated HPG changed the interfacial properties of the particles in the solution. The long molecule chains increased the “water solubility” of particles and protected the particles from congregating [36].

The obtained samples were also characterized by FTIR (Figure 4). The peak observed at wave number 550 cm^{-1} for C-Fe₃O₄ was related to Fe-O bond [37]. The peak at 1071 cm^{-1} belongs to the Si-O stretch band. FTIR spectra of C-Fe₃O₄-SiO₂-HPG and C-Fe₃O₄-SiO₂-HPG-NH₂ showed Fe-O bonds in the 530 cm^{-1} band. Si-O bonds at 1023 cm^{-1} , N-H stretch at 1455 cm^{-1} , C=C tension at 1635 cm^{-1} , C-H tension at 2874 cm^{-1} , and peak at 3338 cm^{-1} - OH confirm the HPG molecular structure [38]. P-O and P=O stresses were seen at 975 cm^{-1} and 1123 cm^{-1} at FTIR spectra of C-Fe₃O₄-SiO₂-HPG-NH₂ and DPAPA conjugated NPs. At 1458 cm^{-1} , an N-H stretch and 1628 cm^{-1} C=O stretch of -COOH groups were observed, which is consistent with the literature [39]. Thus, FTIR studies confirmed the coating of magnetite nanoparticles with a layers of silica, HPG polymers and DPAPA molecules.

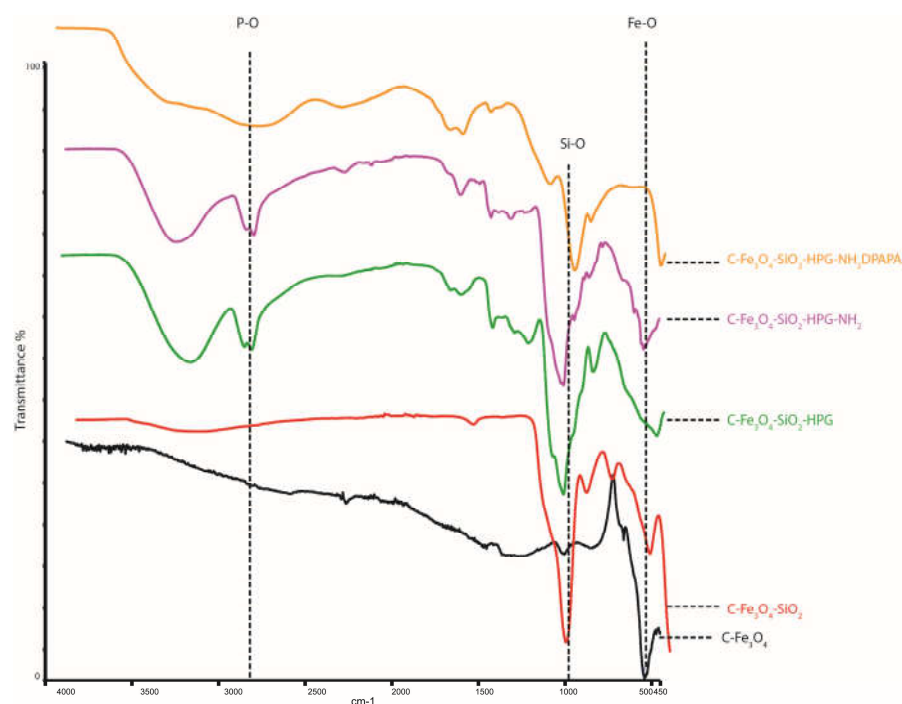


Figure 4. FTIR spectra of NPs and nanoconjugates.

Magnetic properties of nanoparticles and bioconjugates were measured by an applied magnetic field between -3000 and $+3000$ Gauss. The saturation magnetization of the SPION core was 60 emu/g ; however, the coating of the SPIONs with silica and polyglycerol reduces the magnetization significantly. The saturation magnetizations were 25 , and 0.1 emu/g for silica-coated magnetite nanospheres, and HPG-coated nanoconjugates, respectively. NPs exhibited ferrimagnetic characteristics with a small coercivity value [28,33,40]. A similar value 25 emu/g was reported previously [41] for silica-coated magnetite NPs. Xu *et al.* have pointed out that coating with nonmagnetic materials affected the magnitude of magnetization of the coated magnetic materials due to the quenching of surface moments [42]. Because in our studies magnetite NPs were coated with nonmagnetic silica and HPG polymer, a similar mechanism could be considered to decrease

saturation magnetization after silica and HPG coating [28,32]. Unfortunately, the low values of saturation magnetization does not allow the use of synthesized bioconjugates in magnetic hyperthermia therapy.

3.2. ⁴⁴Sc Radiolabeling of Nanoconjugates

The scandium radiolabeling yield was measured using a cyclotron produced nca ⁴⁴Sc. 17.76 MBq ⁴⁴Sc for EDTMP-PSMA and 17.76 MBq ⁴⁴Sc for DPAPA-PSMA were added to NP's and incubated for 30 minutes at 95°C. After incubation, the samples were centrifuged to remove the unbound ⁴⁴Sc from the nanoparticles, and their activities were measured. The radiolabeling efficiency for EDTMP-PSMA was found to be almost 98%. For DPAPA-PSMA, the radiolabeling efficiency was found to be almost 97%.

3.3. Stability of the obtained radiobioconjugates

For stability studies, human serum (HS) and PBS solutions was used. The samples labeled with ⁴⁴Sc were incubated at 37°C. After 1,2,3,4 and 20 hours of incubation samples was measured, then centrifuged, and the supernatant was removed from NPs. NPs without supernatant was measured one more time, and the stability of the connection between NP and Sc was determined. As expected, due to the strong complexation of ⁴⁴Sc by the DOTA ligand, the stability of the radiobioconjugates was high.

Table 2. Stability of the ⁴⁴ Sc labeled C-Fe ₃ O ₄ NC (n=6).					
	1 h	2 h	3 h	4 h	24 h
EDTMP (HS)	93.0	89.7	89.6	90.0	91.7
EDTMP (PBS)	98.9	97.4	97.3	98.3	96.0
DPAPA (HS)	95.3	94.3	92.1	92.2	84.0
DPAPA (PBS)	98.4	96.8	97.4	97.4	92.3

As expected, due to the high thermodynamic and kinetic stability of the DOTA complexes, the stability of the radiobioconjugates was also high.

3.4. Cell Studies

3.4.1. Cell Binding of ^{44}Sc Labeled Bioconjugates

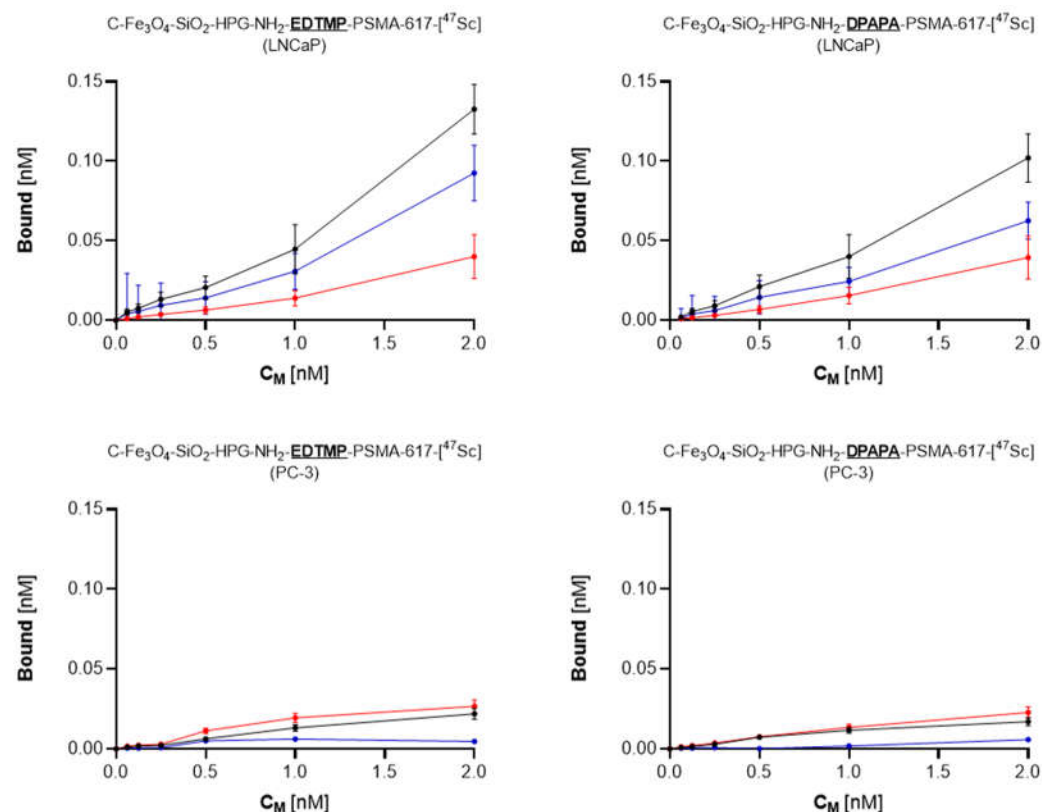


Figure 5. Receptor binding affinity studies of ^{44}Sc labeled EDTMP and DPAPA based radiobiocnjugates. Upper graphs show data for LNCaP cells, bottom graphs are for PC-3 cells.

As presented in Figure 5, both tested compounds bound specifically to PSMA receptors. The significant ($p < 0.05$) decrease in bound fraction confirmed this during the receptor blocking with an excess of PSMA. Either EDTMP and DPAPA-based conjugates showed similar percent of total bound fraction, calculated as 6.6% (EDTMP) and 5.1% (DPAPA), while specifically bound fraction was 4.6% and 3.1% respectively. No binding was observed for PSMA-negative PC-3 cells, which directly shows, that synthesized conjugates were successfully conjugated with PSMA, and its biological activity was maintained. PSMA-617-DPAPA/EDTMP NCs are PSMA receptor specific. Loveless *et al.* showed that PSMA receptors on LNCaP cells were specifically targeted by using [$^{44/47}\text{Sc}$]-PSMA-617 at a molar activity of 10 MBq/nmol [43].

3.4.2. MTT Assay

The percent viabilities decreased with time in PC-3 and LNCaP cell lines (Figure 6). PSMA-617 conjugated nanoconjugates have less toxic effect on cells. PSMA and PSMA conjugated nanoparticles LNCaP cell affinities are relatively higher since LNCaP are PSMA+ prostate cancer cells [44].

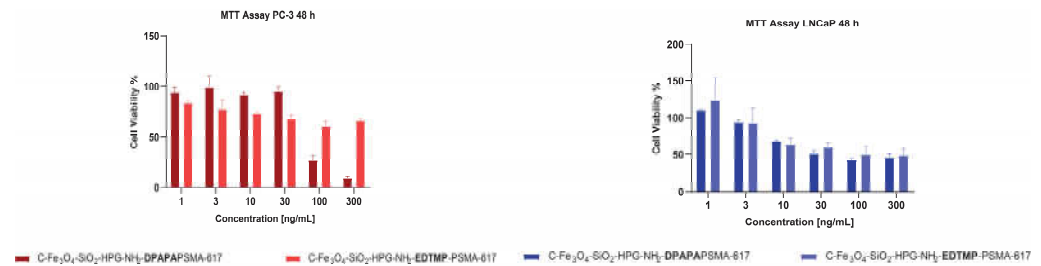


Figure 6. Cell viability of PC-3 and LNCaP cells treated with nanoconjugates after 48 h of incubation.

3.4.3. MTS Assay

Neither EDTMP nor DPAPA conjugates affected mitochondrial activity of LNCaP and PC-3 cells (Figure 7). This agrees with our expectations, because PSMA function is limited to effective targeting without any therapeutic demands due to its low concentration in bioconjugates. We chose non-toxic nanoconjugates concentration, according to data showed in Figure 5 (1 ng/mL). Significant decrease of survival fraction was found after 48 and 72 h incubation of ^{47}Sc labeled radiobioconjugates in LNCaP cells (Figure 7). After 48 h both – EDTMP and DPAPA – induced around 40% decrease of metabolically active cells regardless of the activity concentration ($p \leq 0.01$). Subsequently we found dose-dependent cytotoxicity progression after 72 h. EDTMP-based radiobioconjugates efficacy was variable from $64.14 \pm 5.2\%$ ($p \leq 0.001$) survived fraction (1.25 MBq/mL) to $35.75 \pm 3.2\%$ (20 MBq/mL; $p \leq 0.0001$). DPAPA-based radiobioconjugates were slightly more cytotoxic, and $31.22 \pm 1.9\%$ of cells remained unaffected after 72 h incubation with 20 MBq/mL of ^{47}Sc ($p \leq 0.0001$). Also calculated half maximal inhibitory concentration (IC_{50}) showed that DPAPA-based conjugates were more effective ($\text{IC}_{50} = 5.3 \text{ MBq/mL}$) when compared to EDTMP ($\text{IC}_{50} = 7.1 \text{ MBq/mL}$). Any impact of non-radioactive and radioactive conjugates was found for PC-3 cell line what additionally proves specific anticancer activity only against PSMA(+) cells.

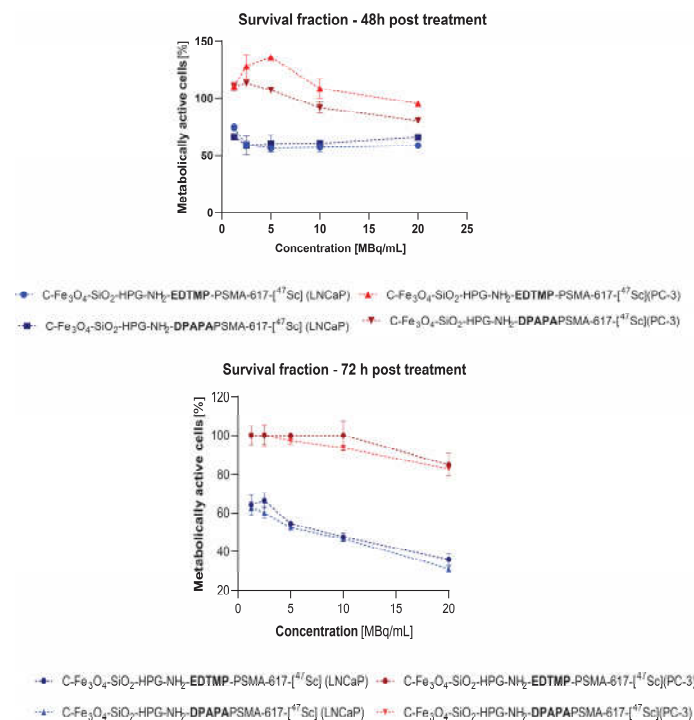


Figure 7. Cell viability of LNCaP and PC-3 cells treated with radiobioconjugates.

3.4.4. Three-dimensional (3D) Cell Culture Studies

According to data obtained during MTS assay (Figure 7) we found slight advantage of DPAPA-based NC over EDTMP-based NC. Taking into account their stronger effect (lower IC_{50} and lower cell viability after 72 h) we decided to investigate DPAPA-based NC against 3D cell cultures. In terms of fluorescence spectra, DPAPA and DPAPA NC nanoconjugates presented fluorescence at 290 nm excitation and 420 nm emission wavelengths. Taking advantage of their green fluorescence properties, these nanoconjugates were applied to the prepared PC-3 and LNCaP 3D spheroids and fluorescence images were obtained (Figure 8).

The image of the nanoconjugates applied to the PC-3 cell line in the green filter can be seen. While cell nuclei are seen with DAPI, the intensely glowing region on the cell wall is thought to be the own fluorescence feature from our nanoconjugates.

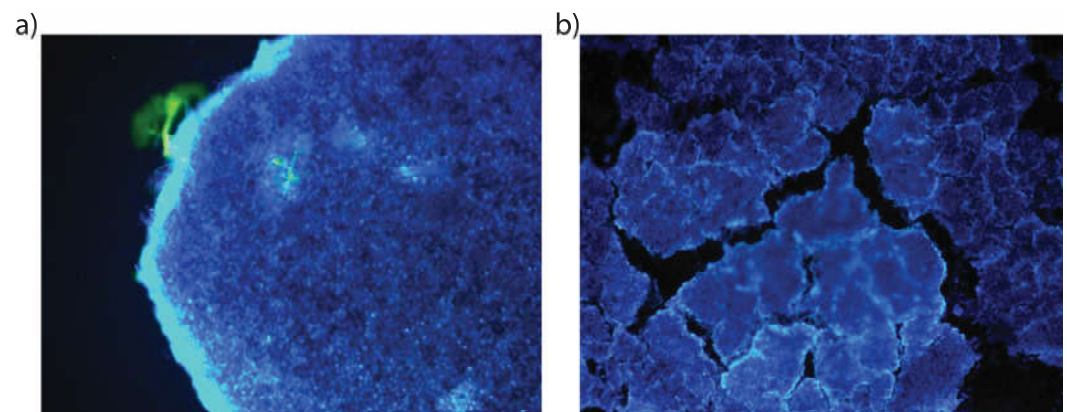


Figure 8. Three-dimensional fluorescence microscope images of a) PC-3 cells (10 X objective magnification green filter) and b) LNCaP cells (10 X objective magnification, blue filter).

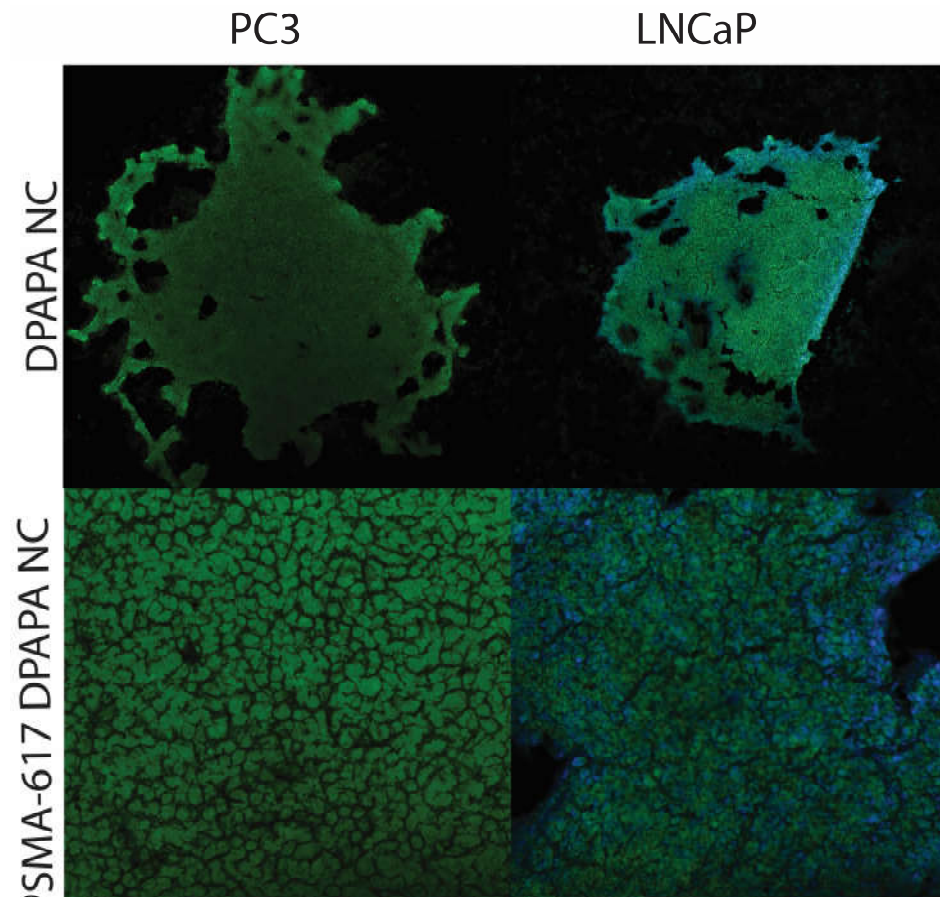


Figure 9. Images of C-Fe₃O₄-SiO₂-HPG-NH₂-DPAPA and C-Fe₃O₄-SiO₂-HPG-NH₂-DPAPA-PSMA-617 applied to PC-3 and LNCaP three-dimensional cell lines (10X objective magnification taken with blue and red filter).

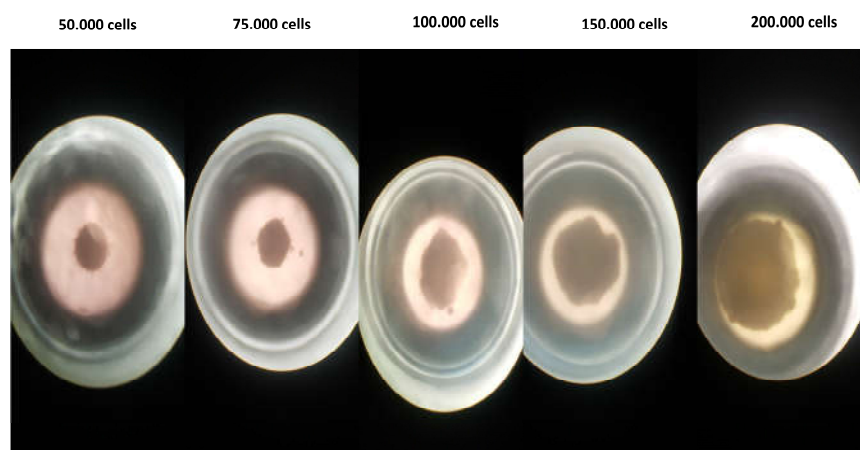


Figure 10. Spheroids images of 3D PC-3 cells (LEICA-DFC280 inverter microscopes, 100X).

Confocal microscopic images of PSMA-617-DPAPA NC and DPAPA NC applied to the PC-3 cells are shown in Figure 9 and Figure 10. In these images, PSMA-617-DPAPA NC and DPAPA NC are green-colored because of the fluorescence property of DPAPA. While DAPI-stained cell nuclei are seen as blue in the cell nucleus. Images are given by overlapping in blue and red filter.

Confocal microscope images were acquired at 500 nm low-resolution and suggested a maximum cell "thickness" of 9.5 μm . which was in excellent quantitative agreement with S.P.M. measurements in the cell nucleus region. These images also showed that the

nanoconjugates were homogeneously distributed in the cell cytoplasm and that DPAPA retained its fluorescence (Figure 9 and Figure 10). DPAPA (similarly to EDTMP) shows fluorescence properties and a report with lanthanide complexes has shown that it can be used in cell imaging by taking advantage of this property [45].

3.4.5. MRI Imaging



Figure 11. Relaxivity (R_2): 0.421/ 3 Tesla Nanoconjugates applied on C- Fe_3O_4 and PC-3 LNCaP) (n=6).

MR contrast measurement presented that the iron contrast can be seen in cell media, although limits are much more significant compared to the PET and SPECT methods (Figure 11). Both SPECT and PET have contrast measurement limits in the picomolar range, while MRI and CT have contrast measurement limits at much higher nmol concentrations [46]. The superior spatial resolution of PET (4–5 mm) makes it more attractive than SPECT (10–15 mm). However, the spatial and temporal resolution of both methods is significantly less than that achieved with MRI or CT. The high sensitivity of nuclear methods combined with the favorable resolution of CT and MRI is the driving force behind hybrid imaging systems such as PET/CT and PET/MRI now available.

The MRI imaging potential of Fe_3O_4 nanoconjugates *in vivo* is essential in terms of adding PET/MRI imaging to the theranostic property of these nanoparticles. In our previous studies, MRI images were taken of prostate tumor-bearing mice given FDG-linked Fe_3O_4 nanoparticles (FDG-MNP), and FDG-MNPs were concentrated in the prostate tumor. At the same time, relatively small amounts were found in organs of other tissues, Particularly the spleen and liver, and FDG-MNP concentrations decreased over time in all tissues [47]. *In vivo* animal MRI images containing Fe_3O_4 and showing the Fe contrast of different conjugate nanoparticles are available in the literature [48,49].

Metastases of prostate cancer cells usually move to the bones. The pelvis and spinal bones are some of the most common areas where prostate cancer spreads. However, radionuclide-labeled phosphonate derivatives are effective for imaging bone metastases and in radionuclide bone pain therapy. While [$^{99\text{m}}\text{Tc}$]Tc-diphosphosphonate imaging are used for imaging, ^{153}Sm or ^{177}Lu radiolabeled EDTMP was applied for radionuclide bone pain therapy. Combining both imaging and treatment with the same agent may be advantageous regarding theranostic potential. Therefore, in this study, a phosphate derivative EDTMP conjugate was added to the nanoconjugate enabling imaging of bone metastases with MR and PET techniques. Another advantage of this approach is to increase the hydrophilicity and solubility of the nanoconjugate.

4. Conclusions

In our work, we proposed a new solution that involves the use of multimodal superparamagnetic iron oxide-based nanoparticles (SPIONs), labeled with two scandium radionuclides, ^{44}Sc and ^{47}Sc , that allow for visualization of the cancer tissue and simultaneous direct irradiation of the tumor. The synthesized nanoparticles were conjugated with biologically active PSMA-617 molecules directing to and recognizing the targeted tumor

tissue. The proposed multimodal SPIONs are advantageous because they will provide successful diagnosis and therapy even for chemo- and radiation resistant tumor cells.

Prostate cancer bone metastases are common in advanced stage of disease. This issue deserves particular attention due to its huge impact on patient management and the recent introduction of many new therapeutic options. Imaging of bone metastases is essential to localize lesions, determine their size and number and examine features and changes during treatment. Therefore, in the present study, the phosphonates EDTMP and DPAPA were added to the nanoconjugate, which enabled MR and PET imaging of bone metastases and palliative therapy with β^- radiation emitted by ^{47}Sc .

We think that a practical effect of our proposal will be the stable magnetic PSMA radiobioconjugate labeled with ^{44}Sc and ^{47}Sc , which after the in vivo studies, could be used for aggressive prostate cancer. We also expect that our results would be helpful in designing other multimodal magnetic radiopharmaceuticals applied in the simultaneous PET and NMR diagnosis, radionuclide therapy.

Author Contributions: Conceptualization, P. Ü.; methodology, P. Ü., V.Y., E.T., K.B.K., R.W., K.W., K.Ż-M., A.M-P.; software, V.Y., E.T. and K.B.K.; formal analysis, P.Ü., V.Y., E.T., K.B.K., R.W., K.W., K.Ż-M. and A.M-P.; investigation, P.Ü., V.Y., E.T., K.B.K., R. W., K.W., K.Ż-M., and A.M-P. ; resources, A. B. and P.Ü.; data curation, V.Y., E.T., K.B.K., R.W. and K.W.; writing P.Ü., V.Y., E.T., K.B.K., R.W., K.W., K.Ż-M., A.M-P and A.B.; original draft preparation, P. Ü., V.Y., E.T., K.B. K., R.W, K. W., K.Ż-M., A.M-P and A.B.; writing—review and editing, , P. Ü., V.Y., E.T., K.B. K., R.W, K. W., K.Ż-M., A.M-P and A.B.; visualization, V. Y.; supervision, P.Ü. and A.B. project administration, P.Ü. and A.B. and funding acquisition, P.Ü. and A.B. All authors have read and agreed to the published version of the manuscript.

Funding: This research was funded by the TUBİTAK Grant 218S749 and POLTUR3/Nanotheran/3/2020 grant founded by National Centre for Research and Development (NCBR), Poland.

Conflicts of Interest: The authors declare no conflict of interest.

References

- Jahandar, M.; Zarrabi, A.; Shokrgozar, M.A.; Mousavi, H. Synthesis, Characterization and Application of Polyglycerol Coated Fe_3O_4 Nanoparticles as a Nano-Theranostics Agent. *Mater Res Express* **2015**, *2*, 125002, doi:10.1088/2053-1591/2/12/125002.
- Lübbe, A.S.; Alexiou, C.; Bergemann, C. Clinical Applications of Magnetic Drug Targeting. *J Surg Res* **2001**, *95*, 200–206, doi:10.1006/jsre.2000.6030.
- Cędrowska, E.; Pruszyński, M.; Gawęda, W.; Żuk, M.; Krysiński, P.; Bruchertseifer, F.; Morgenstern, A.; Karageorgou, M.-A.; Bouziotis, P.; Bilewicz, A. Trastuzumab Conjugated Superparamagnetic Iron Oxide Nanoparticles Labeled with ^{225}Ac as a Perspective Tool for Combined α -Radioimmunotherapy and Magnetic Hyperthermia of HER2-Positive Breast Cancer. *Molecules* **2020**, *25*, 1025, doi:10.3390/molecules25051025.
- Gawęda, W.; Pruszyński, M.; Cędrowska, E.; Rodak, M.; Majkowska-Pilip, A.; Gaweł, D.; Bruchertseifer, F.; Morgenstern, A.; Bilewicz, A. Trastuzumab Modified Barium Ferrite Magnetic Nanoparticles Labeled with Radium-223: A New Potential Radiobioconjugate for Alpha Radioimmunotherapy. *Nanomaterials* **2020**, *10*, 2067, doi:10.3390/nano10102067.
- Żuk, M.; Podgórski, R.; Ruszczyńska, A.; Ciach, T.; Majkowska-Pilip, A.; Bilewicz, A.; Krysiński, P. Multifunctional Nanoparticles Based on Iron Oxide and Gold-198 Designed for Magnetic Hyperthermia and Radionuclide Therapy as a Potential Tool for Combined HER2-Positive Cancer Treatment. *Pharmaceutics* **2022**, *14*, 1680, doi:10.3390/pharmaceutics14081680.
- Chen, J.; Zhu, S.; Tong, L.; Li, J.; Chen, F.; Han, Y.; Zhao, M.; Xiong, W. Superparamagnetic Iron Oxide Nanoparticles Mediated 131I-HVEGF siRNA Inhibits Hepatocellular Carcinoma Tumor Growth in Nude Mice. *BMC Cancer* **2014**, *14*, 114, doi:10.1186/1471-2407-14-114.
- Patel, N.; Duffy, B.A.; Badar, A.; Lythgoe, M.F.; Årstad, E. Bimodal Imaging of Inflammation with SPECT/CT and MRI Using Iodine-125 Labeled VCAM-1 Targeting Microparticle Conjugates. *Bioconj Chem* **2015**, *26*, 1542–1549, doi:10.1021/acs.bioconjchem.5b00380.
- Wang, H.; Kumar, R.; Nagesha, D.; Duclos, R.I.; Sridhar, S.; Gatley, S.J. Integrity of ^{111}In -Radiolabeled Superparamagnetic Iron Oxide Nanoparticles in the Mouse. *Nucl Med Biol* **2015**, *42*, 65–70, doi:10.1016/j.nucmedbio.2014.08.014.
- Azadbakht, B.; Afarideh, H.; Ghannadi-Maragheh, M.; Bahrami-Samani, A.; Yousefnia, H. Absorbed Doses in Humans from ^{188}Re -Rituximab in the Free Form and Bound to Superparamagnetic Iron Oxide Nanoparticles: Biodistribution Study in Mice. *Appl Radiat Isot* **2018**, *131*, 96–102, doi:10.1016/j.apradiso.2017.10.041.

10. Turrina, C.; Oppelt, A.; Mitzkus, M.; Berensmeier, S.; Schwaminger, S.P. Silica-Coated Superparamagnetic Iron Oxide Nanoparticles: New Insights into the Influence of Coating Thickness on the Particle Properties and Lasioglossin Binding. *MRS Commun* **2022**, *12*, 632–639, doi:10.1557/s43579-022-00228-y.
11. Khan, A.; Malik, S.; Bilal, M.; Ali, N.; Ni, L.; Gao, X.; Hong, K. Polymer-Coated Magnetic Nanoparticles. In *Biopolymeric Nanomaterials*; Elsevier, 2021; pp. 275–292.
12. Chapa Gonzalez, C.; Martínez Pérez, C.A.; Martínez Martínez, A.; Olivas Armendáriz, I.; Zavala Tapia, O.; Martel-Estrada, A.; García-Casillas, P.E. Development of Antibody-Coated Magnetite Nanoparticles for Biomarker Immobilization. *J Nanomater* **2014**, *2014*, 1–7, doi:10.1155/2014/978284.
13. Li, M.; Neoh, K.-G.; Wang, R.; Zong, B.-Y.; Tan, J.Y.; Kang, E.-T. Methotrexate-Conjugated and Hyperbranched Polyglycerol-Grafted Fe₃O₄ Magnetic Nanoparticles for Targeted Anticancer Effects. *Eur J Pharm Sci* **2013**, *48*, 111–120, doi:10.1016/j.ejps.2012.10.008.
14. Zhao, S.; Yu, X.; Qian, Y.; Chen, W.; Shen, J. Multifunctional Magnetic Iron Oxide Nanoparticles: An Advanced Platform for Cancer Theranostics. *Theranostics* **2020**, *10*, 6278–6309, doi:10.7150/thno.42564.
15. Mostaghassi, E.; Zarepour, A.; Zarrabi, A. Folic Acid Armed Fe₃O₄-HPG Nanoparticles as a Safe Nano Vehicle for Biomedical Theranostics. *J Taiwan Inst Chem Eng* **2018**, *82*, 33–41, doi:10.1016/j.jtice.2017.11.004.
16. Heydari Sheikh Hossein, H.; Jabbari, I.; Zarepour, A.; Zarrabi, A.; Ashrafizadeh, M.; Taherian, A.; Makvandi, P. Functionalization of Magnetic Nanoparticles by Folate as Potential MRI Contrast Agent for Breast Cancer Diagnostics. *Molecules* **2020**, *25*, 4053, doi:10.3390/molecules25184053.
17. Dendy, P.P. Further Studies on the Uptake of Synkavit and a Radioactive Analogue into Tumour Cells in Tissue Culture. *Br J Cancer* **1970**, *24*, 817–825, doi:10.1038/bjc.1970.96.
18. Lorente, J.A.; Morote, J.; Raventos, C.; Encabo, G.; Valenzuela, H. Clinical Efficacy of Bone Alkaline Phosphatase and Prostate Specific Antigen in the Diagnosis of Bone Metastasis in Prostate Cancer. *J Urol* **1996**, *155*, 1348–1351, doi:10.1016/S0022-5347(01)66263-3.
19. Martinez-Boubeta, C.; Simeonidis, K.; Makridis, A.; Angelakeris, M.; Iglesias, O.; Guardia, P.; Cabot, A.; Yedra, L.; Estradé, S.; Peiró, F.; et al. Learning from Nature to Improve the Heat Generation of Iron-Oxide Nanoparticles for Magnetic Hyperthermia Applications. *Sci Rep* **2013**, *3*, 1652, doi:10.1038/srep01652.
20. Heister, E.; Neves, V.; Tilmaciu, C.; Lipert, K.; Beltrán, V.S.; Coley, H.M.; Silva, S.R.P.; McFadden, J. Triple Functionalization of Single-Walled Carbon Nanotubes with Doxorubicin, a Monoclonal Antibody, and a Fluorescent Marker for Targeted Cancer Therapy. *Carbon N Y* **2009**, *47*, 2152–2160, doi:10.1016/j.carbon.2009.03.057.
21. Sadri, N.; Moghadam, M.; Abbasi, A. MoO₂(Acac)₂@Fe₃O₄/SiO₂/HPG/COSH Nanostructures: Novel Synthesis, Characterization and Catalyst Activity for Oxidation of Olefins and Sulfides. *J Mater Sci: Mater Electron* **2018**, *29*, 11991–12000, doi:10.1007/s10854-018-9301-z.
22. Babu, P.; Sinha, S.; Surolia, A. Sugar–Quantum Dot Conjugates for a Selective and Sensitive Detection of Lectins. *Bioconjug Chem* **2007**, *18*, 146–151, doi:10.1021/bc060204q.
23. Bahrami Samani, A.; Ghannadi-Maragheh, M.; Jalilian, A.; Meftahi, M.; Shirvani, S.; Moradkhani, S. Production, Quality Control and Biological Evaluation of ¹⁵³Sm-EDTMP in Wild-Type Rodents. *Iran J Nucl Med* **2009**, *7*, 12–19.
24. Minegishi, K.; Nagatsu, K.; Fukada, M.; Suzuki, H.; Ohya, T.; Zhang, M.-R. Production of Scandium-43 and -47 from a Powder Calcium Oxide Target via the Nat/⁴⁴Ca(α ,x)-Channel. *Appl Radiat Isot* **2016**, *116*, 8–12, doi:10.1016/j.apradiso.2016.07.017.
25. Pruszyński, M.; Majkowska-Pilip, A.; Loktionova, N.S.; Eppard, E.; Roesch, F. Radiolabeling of DOTATOC with the Long-Lived Positron Emitter ⁴⁴Sc. *Appl Radiat Isot* **2012**, *70*, 974–979, doi:10.1016/j.apradiso.2012.03.005.
26. White, L.D.; Tripp, C.P. Reaction of (3-Aminopropyl)Dimethylethoxysilane with Amine Catalysts on Silica Surfaces. *J Colloid Interface Sci* **2000**, *232*, 400–407, doi:10.1006/jcis.2000.7224.
27. Zhang, P.; Li, Y.; Tang, W.; Zhao, J.; Jing, L.; McHugh, K.J. Theranostic Nanoparticles with Disease-Specific Administration Strategies. *Nano Today* **2022**, *42*, 101335, doi:10.1016/j.nantod.2021.101335.
28. Pourmiri, S.; Tzitzios, V.; Hadjipanayis, G.C.; Meneses Brassea, B.P.; El-Gendy, A.A. Magnetic Properties and Hyperthermia Behavior of Iron Oxide Nanoparticle Clusters. *AIP Adv* **2019**, *9*, 125033, doi:10.1063/1.5130425.
29. Vasić, K.; Knez, Ž.; Konstantinova, E.A.; Kokorin, A.I.; Gyergyek, S.; Leitgeb, M. Structural and Magnetic Characteristics of Carboxymethyl Dextran Coated Magnetic Nanoparticles: From Characterization to Immobilization Application. *React Funct Polym* **2020**, *148*, 104481, doi:10.1016/j.reactfunctpolym.2020.104481.
30. Feuser, P.E.; Bubniak, L. dos S.; Silva, M.C. dos S.; Viegas, A. da C.; Castilho Fernandes, A.; Ricci-Junior, E.; Nele, M.; Tedesco, A.C.; Sayer, C.; de Araújo, P.H.H. Encapsulation of Magnetic Nanoparticles in Poly(Methyl Methacrylate) by Miniemulsion and Evaluation of Hyperthermia in U87MG Cells. *Eur Polym J* **2015**, *68*, 355–365, doi:10.1016/j.eurpolymj.2015.04.029.
31. Honary, S.; Zahir, F. Effect of Zeta Potential on the Properties of Nano-Drug Delivery Systems - A Review (Part 1). *Trop J Pharm Res* **2013**, *12*, doi:10.4314/tjpr.v12i2.19.
32. Çitoğlu, S.; Coşkun, Ö.D.; Tung, L.D.; Onur, M.A.; Thanh, N.T.K. DMSA-Coated Cubic Iron Oxide Nanoparticles as Potential Therapeutic Agents. *Nanomedicine* **2021**, *16*, 925–941, doi:10.2217/nnm-2020-0467.
33. Wang, J.; Zheng, S.; Shao, Y.; Liu, J.; Xu, Z.; Zhu, D. Amino-Functionalized Fe₃O₄@SiO₂ Core–Shell Magnetic Nanomaterial as a Novel Adsorbent for Aqueous Heavy Metals Removal. *J Colloid Interface Sci* **2010**, *349*, 293–299, doi:10.1016/j.jcis.2010.05.010.

34. Shapiro, E.M.; Skrtic, S.; Koretsky, A.P. Sizing It up: Cellular MRI Using Micron-Sized Iron Oxide Particles. *Magn Reson Med* **2005**, *53*, 329–338, doi:10.1002/mrm.20342.
35. Tang, F.; Li, L.; Chen, D. Mesoporous Silica Nanoparticles: Synthesis, Biocompatibility and Drug Delivery. *Adv Mat* **2012**, *24*, 1504–1534, doi:10.1002/adma.201104763.
36. Wang, S.-Y.; Chen, X.-X.; Li, Y.; Zhang, Y.-Y. Application of Multimodality Imaging Fusion Technology in Diagnosis and Treatment of Malignant Tumors under the Precision Medicine Plan. *Chin Med J (Engl)* **2016**, *129*, 2991–2997, doi:10.4103/0366-6999.195467.
37. Yasakci, V.; Tekin, V.; Guldu, O.K.; Evren, V.; Unak, P. Hyaluronic Acid-Modified [19F]FDG-Conjugated Magnetite Nanoparticles: In Vitro Bioaffinities and HPLC Analyses in Organs. *J Radioanal Nucl Chem* **2018**, *318*, 1973–1989, doi:10.1007/s10967-018-6282-6.
38. Sigma-Aldrich IR Spectrum Table & Chart Available online: <https://www.sigmaaldrich.com/PL/pl/technical-documents/technical-article/analytical-chemistry/photometry-and-reflectometry/ir-spectrum-table> (accessed on 15 February 2023).
39. Hampton, C.; Demoin, D. *Vibrational Spectroscopy Tutorial: Sulfur and Phosphorus*; Fall 2010 Organic Spectroscopy Dr. Rainer E. Glaser
40. Bekiş, R.; Medine, İ.; Dağdeviren, K.; Ertay, T.; Ünak, P. A New Agent for Sentinel Lymph Node Detection: Preliminary Results. *J Radioanal Nucl Chem* **2011**, *290*, 277–282, doi:10.1007/s10967-011-1250-4.
41. Medine, E.I.; Ünak, P.; Sakarya, S.; Özkaya, F. Investigation of in Vitro Efficiency of Magnetic Nanoparticle-Conjugated 125I-Uracil Glucuronides in Adenocarcinoma Cells. *J Nanopart Res* **2011**, *13*, 4703–4715, doi:10.1007/s11051-011-0436-6.
42. Xu, Y.H.; Bai, J.; Wang, J.-P. High-Magnetic-Moment Multifunctional Nanoparticles for Nanomedicine Applications. *J Magn Magn Mater* **2007**, *311*, 131–134, doi:10.1016/j.jmmm.2006.11.174.
43. Loveless, C.S.; Blanco, J.R.; Diehl, G.L.; Elbahrawi, R.T.; Carzaniga, T.S.; Braccini, S.; Lapi, S.E. Cyclotron Production and Separation of Scandium Radionuclides from Natural Titanium Metal and Titanium Dioxide Targets. *J Nucl Med* **2021**, *62*, 131–136, doi:10.2967/jnumed.120.242941.
44. Xing, Y.; Xu, K.; Li, S.; Cao, L.; Nan, Y.; Li, Q.; Li, W.; Hong, Z. A Single-Domain Antibody-Based Anti-PSMA Recombinant Immunotoxin Exhibits Specificity and Efficacy for Prostate Cancer Therapy. *Int J Mol Sci* **2021**, *22*, 5501, doi:10.3390/ijms22115501.
45. Li, R.; Ji, Z.; Dong, J.; Chang, C.H.; Wang, X.; Sun, B.; Wang, M.; Liao, Y.-P.; Zink, J.I.; Nel, A.E.; et al. Enhancing the Imaging and Biosafety of Upconversion Nanoparticles through Phosphonate Coating. *ACS Nano* **2015**, *9*, 3293–3306, doi:10.1021/acsnano.5b00439.
46. Sadeghi, M.M.; Glover, D.K.; Lanza, G.M.; Fayad, Z.A.; Johnson, L.L. Imaging Atherosclerosis and Vulnerable Plaque. *J Nucl Med* **2010**, *51*, 51S–65S, doi:10.2967/jnumed.109.068163.
47. Aras, O.; Pearce, G.; Watkins, A.J.; Nurili, F.; Medine, E.I.; Guldu, O.K.; Tekin, V.; Wong, J.; Ma, X.; Ting, R.; et al. An In-Vivo Pilot Study into the Effects of FDG-MNP in Cancer in Mice. *PLoS One* **2018**, *13*, e0202482, doi:10.1371/journal.pone.0202482.
48. Kim, B.M.; Lee, D.R.; Park, J.S.; Bae, I.; Lee, Y. Liquid Crystal Nanoparticle Formulation as an Oral Drug Delivery System for Liver-Specific Distribution. *Int J Nanomedicine* **2016**, *853*, doi:10.2147/IJN.S97000.
49. Arias-Ramos, N.; Ibarra, L.E.; Serrano-Torres, M.; Yagüe, B.; Caverzán, M.D.; Chesta, C.A.; Palacios, R.E.; López-Larrubia, P. Iron Oxide Incorporated Conjugated Polymer Nanoparticles for Simultaneous Use in Magnetic Resonance and Fluorescent Imaging of Brain Tumors. *Pharmaceutics* **2021**, *13*, 1258, doi:10.3390/pharmaceutics13081258.